2000

Kinematic structure of minipermeameter flow

Daniel M. Tartakovsky
Los Alamos National Laboratory

J. David Moulton
Los Alamos National Laboratory

Vitaly A. Zlotnik
University of Nebraska-Lincoln, vzlotnik1@unl.edu

WATER RESOURCES RESEARCH, VOL. 36, NO. 9, PAGES 2433–2442, SEPTEMBER 2000

Kinematic structure of minipermeameter flow

Daniel M. Tartakovsky
Computer Research and Applications Group, Los Alamos National Laboratory, Los Alamos, New Mexico

J. David Moulton
Mathematical Modeling and Analysis Group, Los Alamos National Laboratory, Los Alamos, New Mexico

Vitaly A. Zlotnik
Department of Geosciences, University of Nebraska, Lincoln

Abstract. Minipermeameters are rapidly becoming a popular tool for collecting localized measurements of permeability in both laboratory and field studies. While one of the main advantages of minipermeameters is their ability to collect data on various support volumes, there have been only limited attempts to analyze their size and geometry. We define the support volume of minipermeameter measurements as a region containing 90% of the total gas flow, i.e., a region bounded by the 10% streamline. Using our new semianalytical solutions for the Stokes' stream function, we demonstrate that the support volume has a shape of the semitoroid adjacent to the sample surface. Hence there is a blind spot directly below the minipermeameter, which is not probed by the measurement. We demonstrate that the support volume of the minipermeameter measurements decreases with the tip-seal's ratio (a ratio of the inner tip-seal radius to the outer tip-seal radius), while the size of the corresponding blind spot increases.

1. Introduction

Delineation of the spatial distribution of permeability in water- and oil-bearing formations is one of the major challenges in hydrogeology and petroleum engineering. Specifically, this is an ill-posed inverse problem, and hence it is inherently difficult to solve. Mathematical models that provide a means to extract permeability data indirectly from experimental measurements of dependent quantities (e.g., pressure head and flow rates) do so by defining a related well-posed problem through some form of regularization. The necessary presence of this regularization, which may not be stated explicitly, is likely a critical factor in the recent debate over the scale dependence of permeability measurements. Consequently, there is a growing interest in experimental procedures that possess well-defined regions of investigation or support volumes.

Minipermeameters seem well suited for this purpose because they induce a localized flow by injecting gas into a sample through a small tip seal. Although these devices were first described by *Dykstra and Parsons* [1950], it was not until recently that *Goggin et al.* [1988] proposed a mathematical model for the application of the minipermeameter to localized permeability measurements. In particular, for the case of steady state gas flow, *Goggin et al.* [1988] introduced a coefficient of proportionality into an integral form of Darcy's law. Dubbed the geometric factor, this coefficient allowed the permeability to be inferred from the injection rate and the corresponding gas pressure. The experimental aspect of this work focused on measuring the permeability of core samples; thus the support volume was defined by the sensitivity of the geometric factor to the sample size. Specifically, the support volume was determined by numerically studying the convergence of the geometric factor for samples of increasing size to the geometric factor for the infinite half-space.

Similarly, *Suboor and Heller* [1995] investigated the support volume of the minipermeameter experimentally by conducting a series of measurements over a large sample of Berea sandstone. An interesting part of this research considered the influence of both permeable and impermeable boundary conditions in an effort to emulate the influence of heterogeneities. *Young* [1989] explored the anisotropy effects on permeability measurements and support volumes. More recently, *Tidwell and Wilson* [1997] observed that sample boundaries located within a distance of 2.5–4.0 inner radii of the minipermeameter tip can skew its response by as much as 10%.

Several other researchers have also conducted experimental studies of the minipermeameter and the geometric factor model. For example, *Mitlin and McLennan* [1997] studied its extension to transient experiments, and *Vandewaal et al.* [1998] estimated the inertial effects of several commonly used gases. To demonstrate the ability of this model to delineate experimental data that has been collected on different support volumes, *Tidwell and Wilson* [1997] used different sized tip seals in their minipermeameter experiments. By treating the minipermeameter as a linear filter, *Tidwell et al.* [1999] employed weighting functions to analyze experimental data collected from heterogeneous samples.

Despite a significant number of experimental studies and an increasing number of practical applications (for a detailed review see *Hurst and Goggin* [1995]), considerable uncertainty regarding the support volume of the minipermeameter still remains. Common to these studies is the assertion that the support volume or measurement scale is defined as the characteristic length of the device at which the measured response is no longer sensitive to boundaries or properties of the porous

Paper number 2000WR900178.
0043-1397/00/2000WR900178$09.00

media [*Goggin et al.*, 1988; *Winterbottom*, 1990; *Suboor and Heller*, 1995]. However, because of the complex nonuniform flow induced by the minipermeameter, this definition may be inadequate. In particular, the focus has been on the sensitivity of the geometric factor and on the pressure distribution (pseudopotential) in the sample, while the kinematic flow structure (streamlines) has been largely ignored. Yet the behavior of streamlines provides significant insight into this complex flow by identifying the zones of most intensive flow. Hence one can define the support volume as a zone bounded by the streamline encompassing a significant fraction (e.g., 90%) of the total flow between the device and atmosphere. This alternative definition of the support volume was proposed by *Zlotnik and Ledder* [1996] to evaluate the support scale of the steady state dipole-flow test and used by *Peursem et al.* [1998, 1999] to characterize the kinematic flow structure of similar recirculatory flow systems. Further emphasizing that to correctly determine the experiments' support volume, as well as the influence that this quantity has on the inferred permeability, a thorough understanding of the flow structure is necessary.

The analyses of permeameter models may be divided into two categories: the finite-domain case, which applies to small samples, and the infinite-domain case, which applies to sufficiently large samples or measurements in the field. In the first case, numerical simulations provide a natural approach to investigate the flow structure. To the best of our knowledge, the first numerical simulation of the single-phase steady state gas pressure distribution was conducted by *Goggin et al.* [1988]. This is a relatively low-resolution simulation study that used a nonconservative discretization of the underlying partial differential equation. Some adaptivity in the mesh was used to minimize the influence of the nonconservative scheme, and it is clear that qualitatively the gas pressure distribution is reasonable. However, the influence of the singularities in the pressure gradient, which appear at the edges of the tip seal, has not been resolved. In particular, a highly resolved and accurate numerical simulation is necessary to evaluate the flow structure, and hence the support volume, of the minipermeameter. We note that subsequent numerical investigations dealt with transient gas flow [*Jones*, 1992] and with effects of the residual water saturation [*Daltaban et al.*, 1991]].

In contrast, more analytic tools may be applied in the infinite-domain case. In fact, to gain physical insight into this phenomena, analytical or semianalytical solutions prove to be invaluable. Unfortunately, solving the boundary value problem analytically for the gas pressure (or gas pseudopotential) distribution in the vicinity of a minipermeameter is complicated by the presence of the mixed boundary conditions. Indeed, along the surface of a sample, gas pressure is constant inside the injection tip and in the region open to the atmosphere, and the pressure gradient is zero across the tip seal. A similar problem was encountered by *Muskat* [1937], who considered flow toward partially penetrating wells. These problems are often solved by transforming the governing differential equations into the integral Fredholm equations of the first kind which are commonly ill-posed [see, e.g., *Dagan*, 1978; *Goggin et al.*, 1988; *Cole and Zlotnik*, 1994; *Cassiani and Kabala*, 1998]. Alternatively, one can transform the governing equations into a system of the well-posed Fredholm equations of the second kind [*Cooke*, 1963; *Ufliand*, 1977]. In turn, the auxiliary functions given by the solutions of these Fredholm equations are used to define the solution of the original differential equation. This is the approach we pursue here.

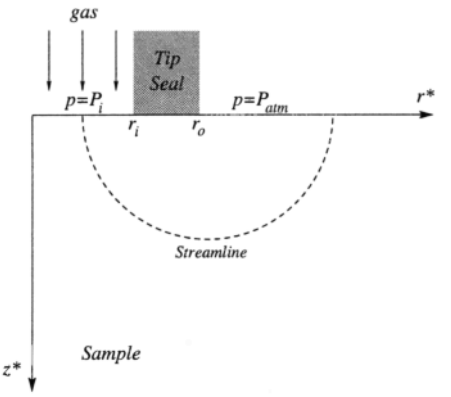

Figure 1. Schematic of the minipermeameter configuration.

The main objective of our investigation is to enhance the understanding of the minipermeameter device through a semianalytic study of the linearized gas model over an infinite half-space. We begin by introducing the flow model in section 2. Next we develop analytic expressions for the pseudopotential (section 2.2) and the Stokes' stream function (section 2.3). The numerical methods that we used to evaluate these expressions are described in section 3. In section 4 we present our results and discuss the flow structure and the support volume of the minipermeameter. We also discuss the geometric factor and anisotropic media. Finally, our concluding remarks are given in section 5.

2. Statement of the Problem

Minipermeameters are often used to collect permeability data on a compact support volume. A typical minipermeameter operates by injecting gases, such as compressed nitrogen [*Goggin et al.*, 1988], into a permeable sample under a constant pressure $p = P_i$. The gas is injected through a circular tip with inner radius r_i. A tip seal of outer radius r_o ($r_i < r_o$) is used to prevent gas leakage between the injection tip and the sample surface (Figure 1). Outside the tip seal ($r > r_o$) the sample's surface is open to the atmosphere, and thus the pressure at this surface is the atmospheric pressure $p = P_{\text{atm}}$. Without loss of generality we shift this pressure to zero. Since minipermeameters collect data on small support volumes, it is reasonable to assume that the material sample is much larger than the flow domain (i.e., mathematically we assume that the material sample is infinite).

Isothermal steady state flow of a gas with temperature T, molecular weight M, viscosity $\mu(p)$, compressibility factor $Z(p)$, and slippage coefficient β is conveniently described by the real gas pseudopotential [e.g., *Tartakovsky*, 1999],

$$\Phi^*[p] = \frac{M}{RT}\int_0^p \frac{s+\beta}{\mu(s)Z(s)}\,ds, \tag{1}$$

where R is the universal gas constant. In particular, the mass flux $\mathbf{q}^* = (q_r^*, q_z^*)^T$ may be expressed in the familiar form

$$q_r^* = -K_r\frac{\partial \Phi^*}{\partial r^*}, \tag{2a}$$

$$q_z^* = -K_z\frac{\partial \Phi^*}{\partial z^*}, \tag{2b}$$

where K_r and K_z are the permeabilities in r^* and z^* directions, respectively.

2.1. Boundary Value Problem

Combining Darcy's law (2) with conservation of mass and assuming an homogeneous medium with azimuthal symmetry in cylindrical coordinates (r^*, z^*) gives

$$K_r \frac{1}{r^*} \frac{\partial}{\partial r^*} \left[r^* \frac{\partial \Phi^*(r^*, z^*)}{\partial r^*} \right] + K_z \frac{\partial^2 \Phi^*(r^*, z^*)}{\partial z^{*2}} = 0. \tag{3}$$

Along the sample surface, $z^* = 0$,

$$\Phi^* = \Phi_i^* \qquad 0 < r^* < r_i, \tag{4a}$$

$$\frac{\partial \Phi^*}{\partial z^*} = 0 \qquad r_i < r^* < r_o, \tag{4b}$$

$$\Phi^* = 0 \qquad r_o < r^* < \infty, \tag{4c}$$

where Φ_i^* is the gas pseudopotential at the injection interval, the Kirchhoff transform of P_i. The flow symmetry with respect to $r^* = 0$ implies that

$$\frac{\partial \Phi^*}{\partial r^*} = 0 \qquad r^* = 0 \quad 0 < z^* < \infty. \tag{4d}$$

Since the sample remains unaffected by the experiment far away from the injection tip, we have

$$\lim_{z^* \to \infty} \Phi^* = 0 \qquad 0 < r^* < \infty, \tag{4e}$$

$$\lim_{r^* \to \infty} \Phi^* = 0 \qquad 0 < z^* < \infty. \tag{4f}$$

Introducing the dimensionless variables

$$r = \frac{r^*}{r_o} \qquad z = \sqrt{\frac{K_r}{K_z}} \frac{z^*}{r_o} \qquad \varepsilon = \frac{r_i}{r_o} \tag{5a}$$

and the scaled pseudopotential function

$$\Phi(r, z) = \frac{\Phi^*(r^*, z^*)}{\Phi_i^*} \tag{5b}$$

gives

$$\frac{1}{r} \frac{\partial}{\partial r} \left[r \frac{\partial \Phi(r, z)}{\partial r} \right] + \frac{\partial^2 \Phi(r, z)}{\partial z^2} = 0, \tag{6}$$

subject to the boundary conditions

$$\Phi = 1 \qquad 0 < r < \varepsilon \quad z = 0, \tag{7a}$$

$$\frac{\partial \Phi}{\partial z} = 0 \qquad \varepsilon < r < 1 \quad z = 0, \tag{7b}$$

$$\Phi = 0 \qquad 1 < r < \infty \quad z = 0, \tag{7c}$$

$$\frac{\partial \Phi}{\partial r} = 0 \qquad r = 0 \quad 0 < z < \infty \tag{7d}$$

and the decay conditions at infinity

$$\lim_{z \to \infty} \Phi = 0 \qquad 0 < r < \infty, \tag{7e}$$

$$\lim_{r \to \infty} \Phi = 0 \qquad 0 < z < \infty. \tag{7f}$$

Therefore, to characterize the properties of the minipermeameter, we will investigate the properties of the pseudopotential Φ that are defined by (6) subject to (7a)–(7f). Although (6) is a linear partial differential equation, its solution is complicated by the combination of different boundary condition types along the surface $z = 0$ (i.e., Dirichlet, Neumann, and Dirichlet), which thwarts standard analytic methods, and the semi-infinite domain, which hinders a direct numerical approach.

2.2. Pseudopotential Function

The general solution of (6) has the form [*Sneddon*, 1966, equation (3.1.2)]

$$\Phi(r, z) = \int_0^\infty A(\xi) \exp(-\xi z) J_0(\xi r)\, d\xi, \tag{8}$$

where J_0 is the zeroth order Bessel function of the first kind and $A(\xi)$ is an arbitrary function to be determined. Note that (8) satisfies the boundary conditions (7d)–(7f) automatically, and therefore $A(\xi)$ is determined by (7a)–(7c).

We show in Appendix A that $A(\xi)$ is given by

$$A(\xi) = \varepsilon \int_0^1 \frac{\lambda \phi_i(\lambda)}{\sqrt{1 - \lambda^2}} J_0(\varepsilon \xi \lambda)\, d\lambda + \int_0^1 \frac{\phi_o(\mu)}{\sqrt{1 - \mu^2}} J_0\left(\frac{\xi}{\mu}\right) d\mu, \tag{9}$$

where the functions $\phi_i(\lambda)$ and $\phi_o(\mu)$ are the solutions of a system of Fredholm integral equations of the second kind,

$$\phi_i(\lambda) = \frac{2}{\pi} - \frac{2}{\pi} \int_0^1 \mathcal{B}(\lambda, \sigma; \varepsilon) \phi_o(\sigma)\, d\sigma, \tag{10a}$$

$$\phi_o(\mu) = -\frac{2\varepsilon}{\pi} \int_0^1 \mathcal{B}(\mu, \tau; \varepsilon) \phi_i(\tau)\, d\tau. \tag{10b}$$

Here $0 \le \lambda \le 1$, $0 \le \mu \le 1$, and the kernel $\mathcal{B}$ is given by

$$\mathcal{B}(x, y; \varepsilon) = \frac{\sqrt{1 - (\varepsilon y)^2}}{1 - (\varepsilon x y)^2} \frac{y}{\sqrt{1 - y^2}}. \tag{11}$$

Therefore solving (10) uniquely determines the distribution of the pseudopotential $\Phi(r, z)$.

2.3. Stokes' Stream Function

Stokes' stream function, $\Psi^*(r^*, z^*)$, is defined by the following relations [*Bear*, 1972, p. 229]:

$$\frac{\partial \Psi^*}{\partial r^*} = -K_z r^* \frac{\partial \Phi^*}{\partial z^*}, \tag{12a}$$

$$\frac{\partial \Psi^*}{\partial z^*} = K_r r^* \frac{\partial \Phi^*}{\partial r^*}, \tag{12b}$$

subject to $\Psi^*(0, 0) = 0$. Level curves of Ψ^* represent streamlines, and hence this function provides a natural mechanism for analyzing flow structure.

Using dimensionless quantities (5) and introducing the dimensionless Stokes' stream function,

$$\Psi(r, z) = \frac{\Psi^*(r^*, z^*)}{\Phi_i^* r_o \sqrt{K_r K_z}}, \tag{13}$$

yields

$$\frac{\partial \Psi}{\partial r} = -r \frac{\partial \Phi}{\partial z}, \tag{14a}$$

$$\frac{\partial \Psi}{\partial z} = r \frac{\partial \Phi}{\partial r}, \tag{14b}$$

where we now have the condition $\Psi(0, 0) = 0$. Hence it follows from (8) that Stokes' stream function, in general form, is given by

$$\Psi(r, z) = r \int_0^\infty A(\xi) \exp(-\xi z) J_1(\xi r)\, d\xi, \tag{15}$$

and therefore it is uniquely determined by $A(\xi)$.

3. Numerical Methods

We are interested in the behavior of both the pseudopotential and the stream function over the (r, z) plane. We are particularly interested in the dependence of measurable quantities on the device parameter ε and in the solution near the singular points $(r_i, 0)$ and $(r_o, 0)$. In this section we develop expressions for these quantities that are suitable for numerical computation and comment on their evaluation.

3.1. Solving the Integral Equations

One possible approach to solving the system of integral equations given in (10) is to apply the standard Nystrom method [e.g., see *Delves and Mohamed*, 1985]. However, in this case analytically decoupling the equations proves to be a very nice simplification that significantly reduces the solution cost. First, substitution of (10b) into (10a) yields a single equation for $\phi_i(\lambda)$, and second, substitution of (10a) into (10b) yields a single equation for $\phi_o(\mu)$. This decoupled system may be written as

$$\phi_i(\lambda) = \frac{2}{\pi} + \frac{4}{\pi^2} \int_0^1 \hat{\mathcal{B}}(\lambda, \sigma; \varepsilon) \phi_i(\sigma)\, d\sigma, \tag{16a}$$

$$\phi_o(\mu) = \frac{4}{\pi^2} \alpha(\mu; \varepsilon) + \frac{4}{\pi^2} \int_0^1 \hat{\mathcal{B}}(\mu, \tau; \varepsilon) \phi_o(\tau)\, d\tau, \tag{16b}$$

where $0 \le \lambda \le 1$, $0 \le \mu \le 1$, and the kernel is given by

$$\hat{\mathcal{B}}(x, y; \varepsilon) = \varepsilon \int_0^1 \mathcal{B}(x, s; \varepsilon) \mathcal{B}(s, y; \varepsilon)\, ds \tag{17}$$

and the inhomogeneous term is

$$\alpha(\mu; \varepsilon) = -\varepsilon \int_0^1 \mathcal{B}(\mu, \sigma; \varepsilon)\, d\sigma. \tag{18}$$

Now we apply the Nystrom method to (16a) and (16b) independently. We note that all of the integrands contain the integrable endpoint singularity $1/\sqrt{1 - s^2}$ for s the variable of integration. Using uniform abscissae on the interval [0, 1], we treat this term as a weight function for which quadrature weights are computed that integrate cubic polynomials exactly. Alternatively, an additional set of transformations could be introduced to eliminate this endpoint singularity. Using the properties of this transformation and the properties of the transformed system, one can show that $\phi_i(\lambda)$ and $\phi_o(\mu)$ are continuous on [0, 1] for $\varepsilon \neq 1$ [*Delves and Mohamed*, 1985, theorem 4.2.2].

3.2. Computing the Pseudopotential

Having solved for $\phi_i(\lambda)$ and $\phi_o(\mu)$, we are in a position to compute the pseudopotential. We first rewrite (8) in the form

$$\Phi(r, z; \varepsilon) = \Phi_i(r, z; \varepsilon) + \Phi_o(r, z; \varepsilon) \tag{19}$$

and reverse the order of integration to obtain

$$\Phi_i(r, z; \varepsilon) = \varepsilon \int_0^1 \frac{\lambda \phi_i(\lambda)}{\sqrt{1 - \lambda^2}} \mathcal{I}_\Phi(r, z, \varepsilon\lambda)\, d\lambda, \tag{20}$$

$$\Phi_o(r, z; \varepsilon) = \int_0^1 \frac{\phi_o(\mu)}{\sqrt{1 - \mu^2}} \mathcal{I}_\Phi\left(r, z, \frac{1}{\mu}\right) d\mu. \tag{21}$$

Here

$$\mathcal{I}_\Phi(r, z; \delta) = \int_0^\infty e^{-\zeta} J_0(\delta\zeta) J_0(r\zeta)\, d\zeta = \frac{2}{\pi} \gamma \mathcal{K}(2\sqrt{r\delta\gamma}), \tag{22}$$

where $\gamma = \sqrt{z^2 + (r + \delta)^2}$ and $\mathcal{K}(m)$ is the complete elliptic integral of the first kind. To integrate (22), we used the work of *Gradshteyn and Ryzhik* [1980, equation (6.612(3))] and *Abramowitz and Stegun* [1972, equation (8.13.3)]. The complete elliptic integral $\mathcal{K}(m)$ was computed with subroutines from the SLATEC library (K. W. Fong et al., Guide to the SLATEC Common Mathematical Library, 1993, http://www.netlib.org/slatec/guide).

3.3. Computing Stokes' Stream Function

The computation of Stokes' stream function follows similarly from (15), which we rewrite as

$$\Psi(r, z; \varepsilon) = \Psi_1(r, z; \varepsilon) + \Psi_2(r, z; \varepsilon). \tag{23}$$

Once again, reversing the order of integration we obtain

$$\Psi_1(r, z; \varepsilon) = -\varepsilon r \int_0^1 \frac{\lambda \phi_i(\lambda)}{\sqrt{1 - \lambda^2}} \mathcal{I}_\Psi(r, z, \varepsilon\lambda)\, d\lambda, \tag{24}$$

$$\Psi_2(r, z; \varepsilon) = -r \int_0^1 \frac{\phi_o(\mu)}{\sqrt{1 - \mu^2}} \mathcal{I}_\Psi\left(r, z, \frac{1}{\mu}\right) d\mu, \tag{25}$$

where

$$\mathcal{I}_\Psi(r, z; \delta) = \int_0^\infty e^{-\zeta} J_0(\delta\zeta) J_1(r\zeta)\, d\zeta. \tag{26}$$

The interaction of two Bessel functions of different order with variably scaled arguments results in a highly oscillatory and slowly decaying integrand, which, for an arbitrary point (r, z), cannot be integrated analytically and is very difficult to treat

numerically. Thus this numerical integration was performed with the specialized routines developed by *Lucas* [1995].

This approach worked quite well for $z > 0$, although computationally it is significantly more expensive than evaluating the pseudopotential (22). However, for $z \to 0^+$ the numerical quadrature exhibits poor convergence. Fortunately, our primary interest is in the case $z = 0$ (i.e., exit flow), for which further simplifications are possible. Specifically, it follows from the dimensionless form of (2b) and (14a) that

$$q_z(r, z) = -\frac{\partial \Phi}{\partial z}. \tag{27}$$

Hence differentiating (8), letting $z \to 0^+$, using (A2a)–(A2c), and rewriting (A16) and (A17) gives

$$q_z(r, 0) = \begin{cases} \dfrac{1}{\sqrt{\varepsilon^2 - r^2}}\, \phi_i\left(\dfrac{r}{\varepsilon}\right) & 0 \le r < \varepsilon \\ 0 & \varepsilon \le r \le 1 \\ \dfrac{1}{r^2\sqrt{r^2 - 1}}\, \phi_o\left(\dfrac{1}{r}\right) & 1 < r < \infty. \end{cases} \tag{28}$$

In section 3.2 we concluded that $\phi_i(\lambda)$ and $\phi_o(\mu)$ are continuous for $\varepsilon \neq 1$. Therefore (28) shows that $q_z(r, 0)$ has integrable singularities of the form $1/\sqrt{\varepsilon - r}$ as $r \to \varepsilon^-$ and $1/\sqrt{r - 1}$ as $r \to 1^+$.

Similarly, an expression for the stream function at $z = 0$ can be derived by integrating (27),

$$2\pi \int_0^r q_z(r, z) r\, dr = 2\pi[\Psi(r, z) - \Psi(0, z)]. \tag{29}$$

Solving for $\Psi(r, z)$, noting that $\Psi(0, 0) = 0$, taking the limit as $z \to 0^+$, and transforming the range of integration leads to

$$\Psi(r, 0) = \begin{cases} \varepsilon \displaystyle\int_{s_0}^1 \phi_i(\sqrt{1 - s^2})\, ds & 0 \le r < \varepsilon, \\ \Psi_m & \varepsilon \le r \le 1, \\ \Psi_m + \displaystyle\int_{\theta_0}^{\pi/2} \phi_o(\sin(\theta))\, d\theta & 1 < r < \infty, \end{cases} \tag{30}$$

where $s_0 = \sqrt{1 - (r/\varepsilon)^2}$, $\theta_0 = \arcsin(1/r)$, and Ψ_m denotes the maximum of the Stokes' stream function, which is given by

$$\Psi_m(\varepsilon) = \varepsilon \int_0^1 \phi_i(\sqrt{1 - s^2})\, ds. \tag{31}$$

To evaluate the integrals that appear in (30) and (31) we use the compound Simpson's rule with equally spaced abscissae. The interpolation of $\phi_i(\lambda)$ and $\phi_o(\mu)$ utilizes the discrete form of (16a) and (16b).

To facilitate the investigation of the solution's dependence on the tip-seal's size ε, we consider the normalized Stokes' stream function,

$$\psi(r, z) = \frac{\Psi(r, z)}{\Psi_m(\varepsilon)}, \tag{32}$$

whose range, $0 \le \psi(r, z) \le 1$, is independent of ε.

4. Results and Discussion

Computations were performed for the three tip-seal ratios, $\varepsilon = 1/4$, $1/2$, and $3/4$, which cover the range of most practical applications [*Suboor and Heller*, 1995, Table 1]. We begin our discussion by analyzing the flow structure corresponding to the minipermeameter experiment. We then investigate the measurement support volume and integral flow characteristics, such as the mass flux distribution along the injection tip. Finally, we comment on the geometric factor and anisotropic media.

4.1. Flow Structure and Support Volume

Figures 2a–2c show the lines of equal pseudopotential (solid lines) and the Stokes' streamlines (dashed lines). These are normalized with the Kirchhoff transformation (1) of the injection gas pressure P_i and the minimum Ψ_m of the Stokes' stream function (31), respectively. As expected, all flow configurations exhibit a boundary layer along the sample surface ($z = 0$), wherein the equipotentials change their direction from normal to the tip to parallel to the tip ($r = \varepsilon$ and $r = 1$). Consequently, the gradient of the pseudopotential is singular at the edges of the tip seal. These important flow characteristics were not resolved by the low-resolution numerical simulations of *Goggin et al.* [1988, Figure 3]. Moreover, the absence of any numerical artifacts or distortions (e.g., oscillations) in the contours of Figures 2a–2c provides a convincing qualitative measure of the solution's accuracy.

The singularities in the gas flux distribution at the surface of the sample, equivalently the z component of the gradient of the pseudopotential, are shown clearly in Figure 3. Specifically, the flux is virtually uniform in the regions away from the injection tip's edges, but at these points ($r = \varepsilon$ and $r = 1$) it becomes infinite. In section 3.3 our analysis showed that in the vicinity of the tip's inner radius, $r \to \varepsilon^-$, $q_z \sim 1/\sqrt{\varepsilon - r}$ and that in the vicinity of the tip's outer radius, $r \to 1^+$, $q_z \sim 1/\sqrt{r - 1}$.

Further inspection of Figures 2a–2c reveals two distinct flow zones in the vicinity of the permeameter. The first zone is bounded between the sample surface ($z = 0$) and the surface obtained by rotating the streamline $\Psi = 0.1$ about the z axis. As flow is most intense in this zone, we will call it the rapid zone. Despite its small size the rapid zone is a conduit for the majority (90%) of the mass exchange between the permeameter and atmosphere. We note that the approximately semitoroidal shape of the rapid zone suggests that a transformation to toroidal coordinates might lead to an approximate analytical solution for the pressure distribution [*Ufliand*, 1977]. We refer to the region that contains the remainder of the flow as the slow zone. Although of infinite extent, this region is a conduit for only the remaining 10% of the mass flux. Naturally, such a subdivision of the flow domain is somewhat subjective, and a more quantitatively optimal subdivision may be possible through further modeling and experimentation. Nevertheless, the choice of the 10% streamline is reasonable for our purposes.

For the tip-seal ratios shown in Figures 2a–2c, the 10% streamline intersects the injection tip ($z = 0$ and $0 \le r \le \varepsilon$) at a distance of approximately 0.4–0.5 times the inner radius r_i. Because of the divergent flow geometry the rapid zone covers a relatively small portion of the flow domain in the vicinity of the permeameter, which leads to a blind spot directly below the device. To highlight this point, the 10% streamlines are isolated in Figure 4 along with the hemispherical region (dotted line) that has been used to conceptualize the permeameter flow previously by *Goggin et al.* [1988, Figure 2], *Suboor and Heller* [1995, Figure 9], and *Tidwell et al.* [1999, Figure 1]. Clearly, there is a substantial difference between the

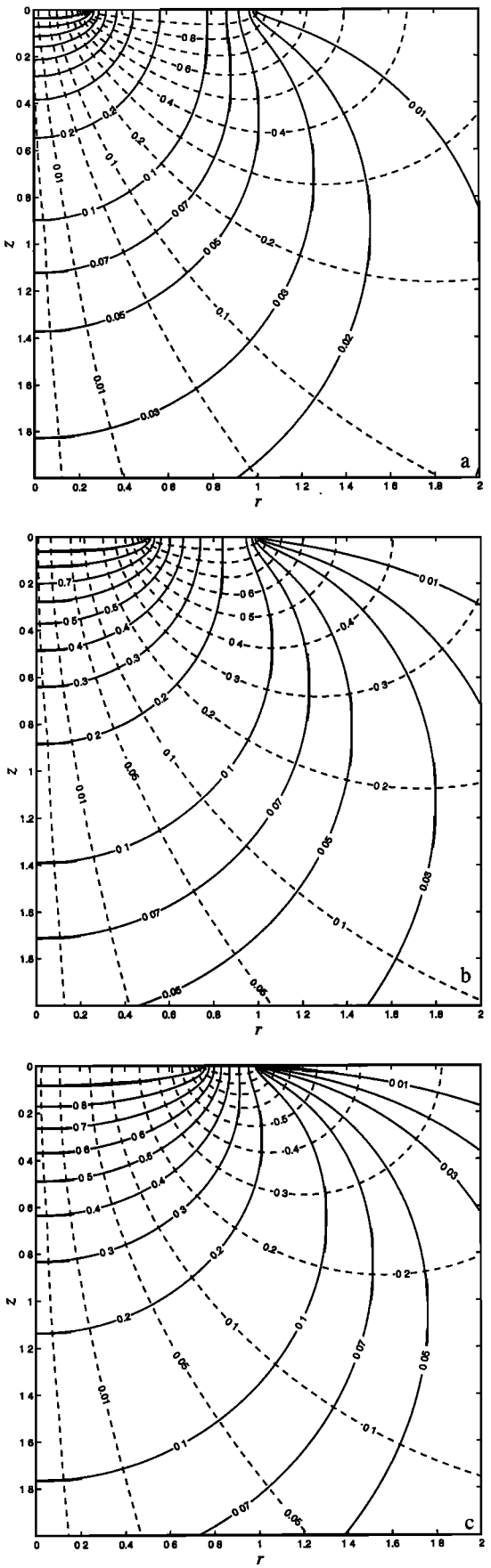

Figure 2. Pseudopotential $\Phi(r, z)$, solid lines, and the Stokes' stream function $\psi(r, z)$, dashed lines, for (a) $\varepsilon = 1/4$, (b) $\varepsilon = 1/2$, and (c) $\varepsilon = 3/4$.

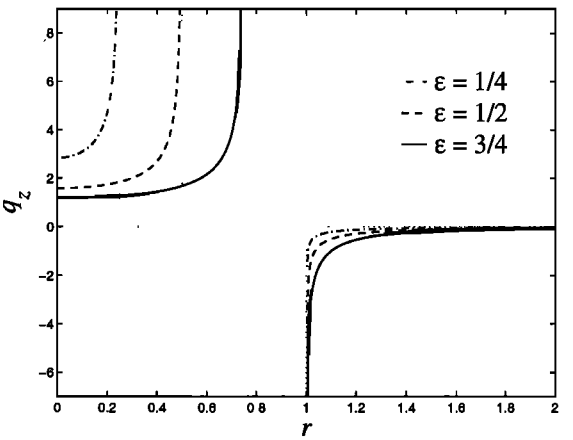

Figure 3. Inflow/outflow profiles, which are singular at the edges of the tip seal, plotted for $\varepsilon = 1/4$, 1/2, and 3/4.

geometries of the rapid zone and a hemisphere defined by the effective radius of *Tidwell et al.* [1999, Figure 10]. This apparent skewing of the rapid zone from the center of the measurement device ($r = 0$) leads one to question the validity of the empirical weighting functions of *Tidwell et al.* [1999, Figure 10], which assigns the largest weight to the region along the $r = 0$ axis. Moreover, it is apparent from Figure 4 that the size of the blind spot increases with the tip-seal ratio, ε.

The existence of such blind spots has a profound implication for the mapping of spatial distributions of permeability. Indeed, for a semi-infinite domain typical of field measurements the local permeabilities that one measures with minipermeameters appear to be more strongly associated with a support volume situated in a semitoroid around the tip seal and not in a hemisphere directly below the device. In contrast, we note that for sufficiently thin samples the blind spot would be reduced, although the half-space geometric factor would not be valid.

4.2. Geometric Factor and Support Volume

The application of the minipermeameter device relies on the geometric factor G_0 to infer a local permeability estimate from a measured gas injection rate. Thus it may seem very natural to

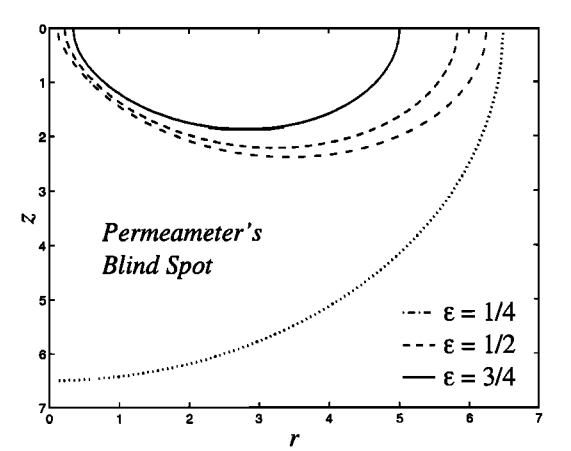

Figure 4. The 10% streamline plotted for three values of the tip-seal ratio, $\varepsilon = 1/4$, 1/2, and 3/4. The hemispherical region is also shown (dotted line) to highlight the potential blind spot of the minipermeameter.

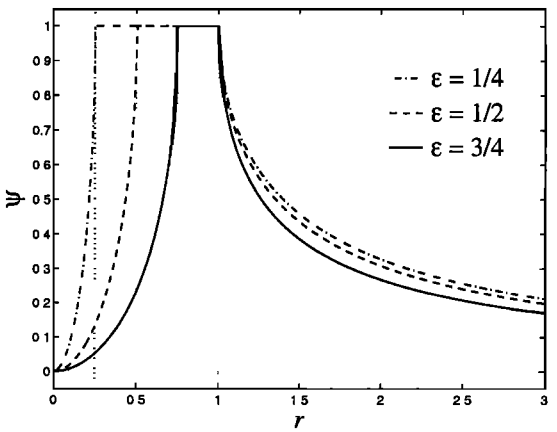

Figure 5. The normalized Stokes' stream function at the sample's surface, $\psi(r, 0)$, plotted for $\varepsilon = 1/4$, 1/2, and 3/4.

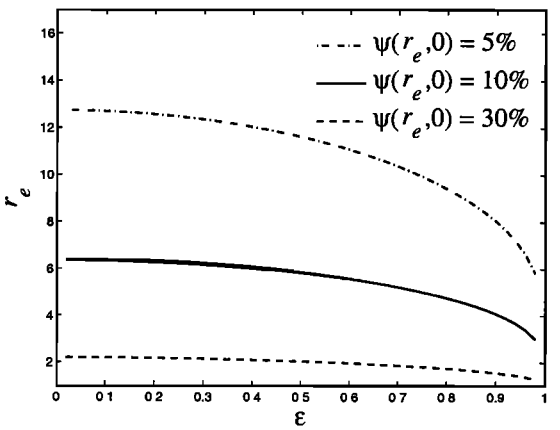

Figure 6. The exit radius of a streamline, $\psi(r_e, 0) = C$, plotted as a function of ε for $C = 5\%$, 10%, and 30%. In all cases, r_e decreases with increasing tip-seal ratio ε.

base estimates of the permeameter's support volume on the sensitivity of G_0 to sample boundaries. However, in general, this approach may be inadequate. In particular, the work of *Goggin et al.* [1988] focused on the convergence of the geometric factor for finite core samples to the geometric factor for the infinite half-space. On the basis of this analysis, *Goggin et al.* [1988, p. 93] found that a sample with both the radius and length equal to 4 times the internal tip radii, $r_s^* = 4r_t$, is effectively infinite. Hence in our dimensionless coordinates this gives a support volume defined by $r_s = 4\varepsilon$. It then follows from Figure 5 that this r_s corresponds to a support volume accounting for only 70% of the total flow for the tip-seal ratio $\varepsilon = 0.5$. Furthermore, noting that this proposed bound has the radius and length equal and that intuitively there is very little flow near the (r_s, z_s) corner of the cylindrical sample, a hemispherical support volume could be defined by this "effective radius" [*Tidwell et al.*, 1999]. However, given the support volume geometry defined by the 10% streamline, this is misleading. In fact, this is precisely where the advantage of using streamlines becomes apparent. While the sensitivity of the geometric factor is important, particularly in applying the infinite half-space values of G_0, an accurate estimate of the geometric factor can, in theory, be computed for any sample size. In contrast, a critical problem in mapping a permeability distribution is determining the volume of the medium that is actually interrogated by the device. Granted, the exact description of a particular streamline may be too complicated to be useful in practice. However, key properties of a particular streamline are readily computed for a range of tip-seal ratios. For example, one can introduce the exit radius r_e of a streamline as a geometric characteristic of the support volume. This exit radius is shown as a function of ε in Figure 6 for the 5%, 10%, and 30% streamlines. This graph reveals that regardless of what fraction of the total flow is used to define the support volume (95%, 90%, or 70%), the exit radius r_e decreases with ε. It also indicates that for $\varepsilon < \sim 0.5$ the simple bound (i.e., $r_e = r_s = 4\varepsilon$) proposed by *Goggin et al.* [1988, p. 93] is not valid.

Other important geometric characteristics of a streamline might include the inlet radius, the maximum depth, and the first radial moment. For example, it is clear from Figure 4 that, similar to the exit radius, the depth decreases with the tip-seal ratio ε. In fact, the depth of investigation is approximately half the exit radius. Hence the support volume of the minipermeameter experiment is located close to the sample surface.

Since the definition of the support volume in terms of the percentage of the total flow is somewhat arbitrary, it might be possible to bound this volume by the 30% rather than the 10% streamline. However, such a definition has a number of potential drawbacks. First, accounting for only 70% of the total flow, it might lead to biased estimates of permeability. Second, it increases the size of the blind spot directly below the tip (Figures 2a–2c), and last, but not least, the 30% streamline is relatively insensitive to the tip's aspect ratio ε (Figure 6). This might be a crucial limitation since varying the aspect ratio is often used to collect permeability data on different supports.

The increasing application of the geometric factor model raises questions beyond the minipermeameter's support volume. For example, what is the physical meaning of G_0? What is the influence of anisotropy and heterogeneities on the measured permeability? Our analysis provides valuable insight into these questions. First, consider the definition of the geometric factor. Following *Goggin et al.* [1988, equation (11)], we examine the total mass flux Q of the gas injected through the circular tip seal,

$$Q = 2\pi \int_0^{r_t} q_z^*(r^*, 0^+) r^* \, dr^*. \tag{33}$$

Substituting q_z^* from (2b) and transforming the integrand to the dimensionless quantities in (5) gives

$$Q = -r_t \sqrt{K_z K_r}\, G_0(\varepsilon) \Phi_t^*, \tag{34}$$

where

$$G_0(\varepsilon) = \frac{2\pi}{\varepsilon} \int_0^{\varepsilon} \left. \frac{\partial \Phi}{\partial z} \right|_{z=0} r \, dr. \tag{35}$$

For isotropic media, *Goggin et al.* [1988, equation (12)] used (35) to define the geometric factor. Combining (35) with the definition of the Stokes' stream function (14a), we arrive at an alternative definition,

$$G_0(\varepsilon) = \frac{2\pi}{\varepsilon} \Psi_m(\varepsilon), \tag{36}$$

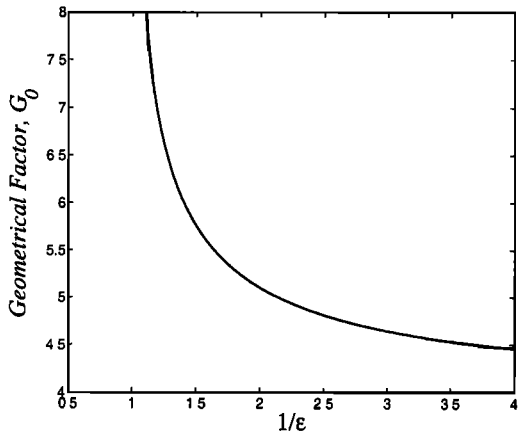

Figure 7. The geometrical factor G_0 computed using the stream function relationship given in equation (36) is in excellent agreement with *Goggin et al.* [1988].

which relates the geometric factor G_0 to the maximum of the stream function. Figure 7 shows the geometric factor evaluated with (36) and is in excellent agreement with *Goggin et al.* [1988, Figure 6], in which their parameter $b_D = 1/\varepsilon$. We emphasize that in contrast to the ill-posed formulation of *Goggin et al.* [1988] we obtain G_0 accurately and efficiently from a well-posed Fredholm integral equation of the second kind.

Second, it is apparent from (34) that inherent in the geometric factor model of the permeameter experiment is the geometric average of the diagonal tensor coefficients, $\sqrt{K_z K_r}$. Although for isotropic media this coefficient reduces to the corresponding scalar permeability, and hence (34) is consistent with *Goggin et al.* [1988, equation 1], its presence implies that a systematic bias in the inferred permeability for anisotropic formations may result from the assumption of isotropy. Nevertheless, this limited model may provide insight into the application of minipermeameters to certain classes of heterogeneous material. In particular, homogenization results (upscaling) could be combined with (34) to analyze layered media. This is relevant to studies such as that of *Suboor and Heller* [1995] in which the support volume depth was investigated experimentally using a two-layer configuration. However, the influence of general anisotropy and general heterogeneous structure is beyond the scope of this model.

5. Conclusions

We investigated the gas flow structure of the minipermeameter experiment by deriving semianalytical solutions for the gas pseudopotential and the stream function. The 10% streamline (the line bounding 90% of the total flow) was used to define the support volume of the experiment. The analysis of our semianalytical solutions leads us to the following major conclusions:

1. The method of double integral equations, which we used to obtain our solution, is computationally efficient and accurate. Unlike previous semianalytical studies, which are based on ill-posed integral equations [e.g., *Goggin et al.*, 1988], our solution is defined by Fredholm equations of the second kind, and thus its formulation is well-posed.

2. The support volume has the form of a semitoroid adjacent to the minipermeameter tip. The support volume covers a relatively small portion of the flow domain in the vicinity of the minipermeameter, which leads to a blind spot directly below the device. The existence of such blind spots has a profound implication for mapping of spatial distributions of permeability.

3. The complex geometry of the support volume makes the reliance on the traditionally used effective radius for its characterization questionable. Instead, one can attempt to characterize such a geometry in terms of the exit radius and depth of investigation. The former is about twice as big as the latter. The size of the support volume decreases with the ratio of the inner to outer radii of the tip.

4. In principle, it is possible to use the different tip-seal ratios for collecting permeability data on varying support volumes. However, one should be aware that the size of the blind spot increases with this parameter.

The concluding observation is regarding the contribution of the local permeability values to the overall estimate from the minipermeameter test. In particular, our work suggests that the width of the stream tube is an indicator of the sensitivity to local heterogeneity. For example, the impact of a small obstruction in the immediate vicinity of the tip seal, or under the tip seal, will effect kinematic flow structure more than the same obstruction near the z axis or deeper in the sample. Quantification of this spatial weighting for heterogeneous media requires a different approach which is beyond the scope of this paper.

Appendix A: Fredholm Equations

In deriving (9)–(11) of section 2.2, we follow a general procedure outlined by *Cooke* [1963]. Substituting (8) into (7a)–(7c), we obtain

$$\int_0^\infty A(\xi) J_0(\xi r)\, d\xi = 1 \qquad 0 \le r \le \varepsilon, \tag{A1a}$$

$$\int_0^\infty \xi A(\xi) J_0(\xi r)\, d\xi = 0 \qquad \varepsilon < r \le 1, \tag{A1b}$$

$$\int_0^\infty A(\xi) J_0(\xi r)\, d\xi = 0 \qquad 1 < r \le \infty. \tag{A1c}$$

We further note that these boundary conditions imply

$$\int_0^\infty \xi A(\xi) J_0(\xi r)\, d\xi = f_i(r) \qquad 0 \le r \le \varepsilon, \tag{A2a}$$

$$\int_0^\infty \xi A(\xi) J_0(\xi r)\, d\xi = 0 \qquad \varepsilon < r \le 1, \tag{A2b}$$

$$\int_0^\infty \xi A(\xi) J_0(\xi r)\, d\xi = f_o(r) \qquad 1 < r \le \infty, \tag{A2c}$$

where $f_i(r)$ and $f_o(r)$ are some unknown functions to be determined. Applying Hankel's inversion theorem to (A2) yields

$$A(\xi) = \int_0^\varepsilon \lambda f_i(\lambda) J_0(\xi\lambda)\, d\lambda + \int_1^\infty \mu f_o(\mu) J_0(\xi\mu)\, d\mu. \tag{A3}$$

Substituting (A3) into (A1a), then changing the order of integration, while noting that

$$\mathcal{J}_i(r, \lambda) = \int_0^\infty J_0(r\xi)J_0(\lambda\xi)\, d\xi$$

$$= \frac{2}{\pi}\int_0^{\min(\lambda, r)} \frac{ds}{\sqrt{\lambda^2 - s^2}\sqrt{r^2 - s^2}}, \quad \text{(A4)}$$

leads, after some algebraic manipulation, to

$$1 - \int_1^\infty \lambda f_o(\lambda)\mathcal{J}_i(r, \lambda)\, d\lambda = \frac{2}{\pi}\int_0^r \int_s^\varepsilon \frac{\lambda f_i(\lambda)\, d\lambda}{\sqrt{\lambda^2 - s^2}\sqrt{r^2 - s^2}}\, ds. \quad \text{(A5)}$$

Equation (A5) is a special case of the Abel type integral equation [*Sneddon*, 1966, equation (2.3.8)],

$$G(x) = \int_x^b \frac{F(t)\, dt}{(t^2 - x^2)^\alpha}, \quad \text{(A6)}$$

where $0 < \alpha < 1$ and $a < x < b$, whose solution is

$$F(t) = -\frac{2}{\pi}\sin(\pi\alpha)\frac{d}{dt}\int_t^b \frac{uG(u)\, du}{(u^2 - t^2)^{1-\alpha}}, \quad \text{(A7)}$$

with $a < t < b$. Hence it follows from (A5) that

$$\sqrt{\varepsilon^2 - \hat{\lambda}^2}\, f_i(\hat{\lambda}) = \frac{2}{\pi} - \frac{2}{\pi}\int_1^\infty \frac{t\sqrt{t^2 - \varepsilon^2}}{t^2 - \hat{\lambda}^2} f_o(t)\, dt, \quad \text{(A8)}$$

where $0 \le \hat{\lambda} \le \varepsilon$.

Substituting (A3) into (A1c), then changing the order of integration, while noting that now

$$\mathcal{J}_o(r, \lambda) = \frac{2}{\pi}\int_{\max(\lambda, r)}^\infty \frac{ds}{\sqrt{s^2 - \lambda^2}\sqrt{s^2 - r^2}}, \quad \text{(A9)}$$

leads, after some algebraic manipulation, to

$$-\int_0^\varepsilon \lambda f_i(\lambda)\mathcal{J}_o(r, \lambda)\, d\lambda = \frac{2}{\pi}\int_r^\infty \int_1^s \frac{\lambda f_o(\lambda)\, d\lambda}{\sqrt{s^2 - \lambda^2}} \frac{ds}{\sqrt{s^2 - r^2}}. \quad \text{(A10)}$$

Taking into account that (A10) is a special case of the Abel type integral equation [*Sneddon*, 1966, equation (2.3.7)],

$$G(x) = \int_a^x \frac{F(t)\, dt}{(x^2 - t^2)^\alpha}, \quad \text{(A11)}$$

whose solution is

$$F(t) = \frac{2}{\pi}\sin(\pi\alpha)\frac{d}{dt}\int_a^t \frac{uG(u)\, du}{(t^2 - u^2)^{1-\alpha}}, \quad \text{(A12)}$$

yields

$$\sqrt{\hat{\mu}^2 - 1}\, f_o(\hat{\mu}) = -\frac{2}{\pi}\int_0^e \frac{s\sqrt{1 - s^2}}{\hat{\mu}^2 - s^2} f_i(s)\, ds, \quad \text{(A13)}$$

where $1 \le \hat{\mu} < \infty$.

Furthermore, we transform the range of integration to (0, 1), in both (A8) and (A13), and we introduce the new parameters (λ, μ) that are consistent with this transformation. Specifically, we define

$$s = \varepsilon\sigma \Rightarrow \hat{\lambda} = \varepsilon\lambda,$$

$$t = 1/\tau \Rightarrow \hat{\mu} = 1/\mu,$$

and after sufficient manipulation we obtain

$$\varepsilon\sqrt{1 - \lambda^2}\, f_i(\lambda\varepsilon) = \frac{2}{\pi} - \frac{2}{\pi}\int_0^1 \frac{\sqrt{1 - (\varepsilon\tau)^2}}{1 - (\varepsilon\lambda\tau)^2}\frac{f_o(1/\tau)}{\tau^2}\, d\tau, \quad \text{(A14)}$$

$$\frac{1}{\mu^2}\sqrt{\frac{1}{\mu^2} - 1}\, f_o\left(\frac{1}{\mu}\right) = -\frac{2}{\pi}\varepsilon^2\int_0^1 \frac{\sigma\sqrt{1 - (\varepsilon\sigma)^2}}{1 - (\varepsilon\mu\sigma)^2} f_i(\varepsilon\sigma)\, d\sigma. \quad \text{(A15)}$$

Defining the new functions

$$\phi_i(\lambda) = \varepsilon\sqrt{1 - \lambda^2}\, f_i(\varepsilon\lambda), \quad \text{(A16)}$$

$$\phi_o(\mu) = \frac{1}{\mu^2}\sqrt{\frac{1}{\mu^2} - 1}\, f_o\left(\frac{1}{\mu}\right) \quad \text{(A17)}$$

and transforming the range of integration to (0, 1), in the second term on the right-hand side of (A3), leads directly to (9)–(11).

Acknowledgments. We are grateful to Stephen Lucas for generously providing his subroutines to evaluate the Bessel function integrals. Also, we thank Alberto Guadagnini and the other referees for their insightful and constructive comments. Finally, we acknowledge our stimulating discussions with John Wilson regarding the practical applications of the minipermeameter.

References

Abramowitz, M., and I. A. Stegun, *Handbook of Mathematical Functions*, Dover, Mineola, N. Y., 1972.

Bear, J., *Dynamics of Fluids in Porous Media*, Elsevier Sci., New York, 1972.

Cassiani, G., and Z. J. Kabala, Hydraulics of a partially penetrating well: Solution to a mixed type boundary value problem via dual integral equations, *J. Hydrol.*, *211*, 100–111, 1998.

Cole, K., and V. A. Zlotnik, Modification of Dagan's numerical method for slug and packer test interpretation, in *Computational Methods in Water Resources X*, vol. 1, edited by A. Peters et al., Kluwer Acad., Norwell, Mass., 1994.

Cooke, J. C., Triple integral equations, *Q. J. Mech. Appl. Math.*, *XVI*, 193–203, 1963.

Dagan, G., A note on packer, slug, and recovery tests in unconfined aquifers, *Water Resour. Res.*, *14*, 929–934, 1978.

Daltaban, T. S., J. S. Wang, and J. S. Archer, Understanding the physics of probe permeameter measurements through the use of the probe permeameter simulation program min-per, in *Minipermeametry in Reservoir Studies: PSTI*, Edinburgh, 1991.

Delves, L. M., and J. L. Mohamed, *Computational Methods for Integral Equations*, Cambridge Univ. Press, New York, 1985.

Dykstra, H., and R. L. Parsons, The prediction of oil recovery by waterflood, in *Secondary Recovery of Oil in the United States*, 2nd ed., pp. 160–174, Am. Pet. Inst., New York, 1950.

Goggin, D. J., R. L. Thrasher, and L. W. Lake, A theoretical and experimental analysis of minipermeameter response including gas slippage and high velocity flow effects, *In Situ*, *12*, 79–116, 1988.

Gradshteyn, I. S., and I. M. Ryzhik, *Tables of Integrals, Series, and Products*, Academic, San Diego, Calif., 1980.

Hurst, A., and D. Goggin, Probe permeability: An overview and bibliography, *AAPG Bull.*, *79*, 463–473, 1995.

Jones, S. C., The profile permeameter: A new, fast, accurate minipermeameter: Spe 24757, paper presented at 67th Annual Technical Conference, Soc. of Pet. Eng., Washington, D. C., 1992.

Lucas, S. K., Evaluating infinite integrals involving products of Bessel functions of arbitrary order, *J. Comput. Appl. Math.*, *64*, 269–282, 1995.

Mitlin, V. S., and J. D. McLennan, Simultaneously measuring permeability and porosity using probe permeameter techniques: A theoretical analysis, *In Situ*, *21*, 187–222, 1997.

Muskat, M., *The Flow of Homogeneous Fluids Through Porous Media*, McGraw-Hill, New York, 1937.

Peursem, D. V., G. Ledder, and V. Zlotnik, The kinematic flow structure for the Gvirtzman-Gorelick in situ voc remediation system, *Transp. Porous Media*, *30*, 363–376, 1998.

Peursem, D. V., V. Zlotnik, and G. Ledder, Groundwater flow near vertical recirculatory well: Effect of skin on flow geometry and travel times with implications for aquifer remediation, *J. Hydrol.*, *222*, 109–122, 1999.

Sneddon, I. N., *Mixed Boundary Value Problems in Potential Theory*, North-Holland, New York, 1966.

Suboor, M. A., and J. P. Heller, Minipermeameter characteristics critical to its use, *In Situ*, *19*, 225–248, 1995.

Tartakovsky, D. M., Prediction of steady-state flow of real gases in randomly heterogeneous porous media, *Physica D*, *133*, 463–468, 1999.

Tidwell, V. C., and J. L. Wilson, Laboratory method for investigating permeability upscaling, *Water Resour. Res.*, *33*, 1607–1616, 1997.

Tidwell, V. C., A. I. Gutjahr, and J. L. Wilson, What does an instrument measure? Empirical spatial weightning functions calculated from permeability data sets measure on multiple sample supports, *Water Resour. Res.*, *35*, 43–54, 1999.

Ufliand, Y. S., *Method of Dual Equations for Problems of Mathematical Physics* (in Russian), Nauka, Moscow, 1977.

Vandewaal, W. W., D. Mikes, and H. Bruining, Inertia factor measurements from pressure-decay curves obtained with probe permeameters, *In Situ*, *22*, 339–371, 1998.

Winterbottom, F. A., Numerical modeling of a minipermeameter, Master's thesis, Heriot-Watt Univ., Edinburgh, Scotland, 1990.

Young, G. R., Determining permeability anisotropy from a core plug using a minipermeameter, Master's thesis, Univ. of Tex., Austin, 1989.

Zlotnik, V., and G. Ledder, Theory of dipole flow in uniform anisotropic aquifers, *Water Resour. Res.*, *32*, 1119–1128, 1996.

J. D. Moulton, Mathematical Modeling and Analysis Group, Los Alamos National Laboratory, Los Alamos, NM 87545. (moulton@lanl.gov)

D. M. Tartakovsky, Computer Research and Applications Group, Los Alamos National Laboratory, Los Alamos, NM 87545. (dmt@lanl.gov)

V. A. Zlotnik, Department of Geosciences, University of Nebraska, Lincoln, NE 68588. (vzlotnik@unl.edu)

(Received November 30, 1999; revised May 4, 2000;
accepted May 25, 2000.)